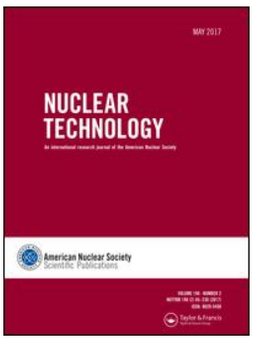

Nuclear Technology

ISSN: 0029-5450 (Print) 1943-7471 (Online) Journal homepage: http://ans.tandfonline.com/loi/unct20

Transmission Electron Microscopy Investigation of Krypton Bubbles in Polycrystalline CeO_2

Lingfeng He, Clarissa Yablinsky, Mahima Gupta, Jian Gan, Marquis A. Kirk & Todd R. Allen

To cite this article: Lingfeng He, Clarissa Yablinsky, Mahima Gupta, Jian Gan, Marquis A. Kirk & Todd R. Allen (2013) Transmission Electron Microscopy Investigation of Krypton Bubbles in Polycrystalline CeO_2, Nuclear Technology, 182:2, 164-169, DOI: 10.13182/NT13-A16428

To link to this article: https://doi.org/10.13182/NT13-A16428

Published online: 10 Aug 2017.

Submit your article to this journal

Article views: 11

Full Terms & Conditions of access and use can be found at
http://ans.tandfonline.com/action/journalInformation?journalCode=unct20

TRANSMISSION ELECTRON MICROSCOPY INVESTIGATION OF KRYPTON BUBBLES IN POLYCRYSTALLINE CeO_2

MATERIALS FOR NUCLEAR SYSTEMS

KEYWORDS: *CeO_2 nuclear fuel, transmission electron microscopy*

LINGFENG HE,[a]* CLARISSA YABLINSKY,[a] MAHIMA GUPTA,[a] JIAN GAN,[b] MARQUIS A. KIRK,[c] and TODD R. ALLEN[a]

[a]*University of Wisconsin-Madison, Department of Engineering Physics Madison, Wisconsin 53706*
[b]*Idaho National Laboratory, Idaho Falls, Idaho*
[c]*Argonne National Laboratory, Argonne, Illinois*

Received June 26, 2012
Accepted for Publication September 28, 2012

To gain an understanding of gas bubble transport in oxide nuclear fuel, this paper uses polycrystalline CeO_2, composed of both nanograins and micrograins, as a surrogate material for UO_2. The CeO_2 was implanted with 150-keV Kr ions up to a dose of 1×10^{16} ions/cm^2 at 600°C. Transmission electron microscopy characterizations of small Kr bubbles in nanograin and micrograin regions were compared. The grain boundary acted as an efficient defect sink, as evidenced by smaller bubbles and a lower bubble density in the nanograin region as compared to the micrograin region.

I. INTRODUCTION

Control of fission gas, both for controlling fuel pellet swelling and for controlling fuel pin pressurization, is a critical component to the performance of any nuclear fuel. Bulk nanostructured materials, such as nanocrystalline (nc) materials,[1,2] nanolayered composites,[3] and nanoparticle-reinforcing steels,[4] have been shown to have improved radiation resistance including low swelling and retention of mechanical strength and ductility compared with their monolithic and polycrystalline counterparts. The improved radiation resistance may be ascribed to their high density of grain boundaries (GBs) or phase interfaces, which serve as sinks for defects of all types. Therefore, the nanostructured materials are very promising for application to nuclear engineering.

Very recently, bulk nc oxides (UO_2, ZrO_2, ThO_2) were suggested by Spino et al.[2] for their potential use as nuclear fuel and inert matrix carriers based on a study of nc-porous 4 mol % Y_2O_3-ZrO_2 (nc-4YTZ), as a surrogate material for high-burnup-structure fuel. The main advantages for nc fuels compared to conventional fuels would be the capacity to develop closed porosity retaining major fission gases (mostly Kr and Xe) and to exhibit higher stress relaxation through higher plasticity.[2] In addition, the improved radiation damage resistance in nc-ZrO_2 has also been reinforced by negligible gas bubble swelling[2] and greatly decreased defect density under ion bombardment.[1]

Because CeO_2 has the same fluorite-type structure and many similar material properties—such as melting temperature and thermal conductivity—as UO_2 and PuO_2, CeO_2 has attracted increasing attention for being a surrogate material for studying UO_2 and PuO_2 fuel.[5–11] The microstructure (bubbles and dislocation loops) evolution under particle bombardment at low dose in CeO_2 is also similar to that in low-burnup UO_2 fuels.[8–11] In this work, polycrystalline CeO_2 composed of both micrograins and nanograins was used as a surrogate material to study the grain size effects on gas bubble transport in nuclear fuels. Transmission electron microscopy (TEM) characterization of polycrystalline CeO_2 irradiated with 150-keV Kr ions at 600°C up to a dose of 1×10^{16} ions/cm^2 was conducted.

*E-mail: lhe33@wisc.edu

II. EXPERIMENTAL

The purity of the polycrystalline CeO_2 pellets[a] is 99.9%, and the density is 6.9 g/cm^3, which is ~96% of the theoretical density. The 3-mm-disk TEM foil was prepared by slicing, mechanical grinding to ~100 μm, dimpling down to ~20 μm using a 15-mm wheel, and ion milling at 4.0 keV to perforation. The final polishing was done with a 3-keV Ar ion beam. The thickness of the outer edge of the prepared TEM foil is ~75 μm. A Kr irradiation was carried out with a Tandem implanter, coupled with a 300-kV Hitachi 9000 NAR transmission electron microscope, at the Intermediate Voltage Electron Microscope–Tandem facility at Argonne National Laboratory (ANL). The 150-keV singly charged Kr ions were selected to produce the desired irradiation damage levels and depths, and the dose rate was 1.5×10^{12} ions/cm$^2 \cdot$s^{-1}. The sample holder in the microscope was heated to irradiation temperature of 600°C and held at 600°C for ~0.5 h before irradiation. The accumulated dose is 1×10^{16} ions/cm^2. To reveal the microstructure of the same CeO_2 sample without Kr implantation, we polished a part of the as-irradiated sample at 600°C to remove the implanted layer, as follows. A small piece of the irradiated foil close to the thick outer edge was cut off, attached to a Mo grid, and made into TEM foil by ion milling at the Kr implanted side. A layer of at least tens of microns in thickness was removed to ensure that only the temperature history of the sample was affected by the irradiation, not the microstructure analyzed. All the TEM micrographs were recorded either with a Philips CM200 microscope at the University of Wisconsin or with a Tecnai F30 microscope equipped with an energy-dispersive spectroscopic (EDS) system at the Center for Advanced Energy Studies, Idaho Falls.

The Stopping and Range of Ions in Matter (SRIM) computer code[12] was used to simulate the profiles of Kr concentration and atomic displacements in CeO_2 as a function of depth. The threshold displacement energies for oxygen and cerium are 20 and 51 eV, respectively.[9,10] The threshold displacement energy used for the Ce sublattice in CeO_2 is the average of the maximum and minimum values estimated from electron irradiation from Yasunaga et al.[9] The SRIM simulation, as shown in Fig. 1, implies that the peak irradiation damage is ~48 displacements per atom (dpa) at a depth of ~25 nm. The gas concentration reaches a peak value of ~2.5 at. % at a depth of 42 nm. If one assumes that the gas concentration increases linearly with depth up to 42 nm, the average gas concentration of a TEM foil with a thickness of 42 nm is ~1.2 at. %. A rough approximation of the burnup (BU) in fuel is 20%, and with 20% of BU being fission gas, it is calculated that the fission gas transmutates from 4 at. % of the total U, which is equivalent to a total fission gas percent of 1.3 at. % within a comparable region in the UO_2 pellet.

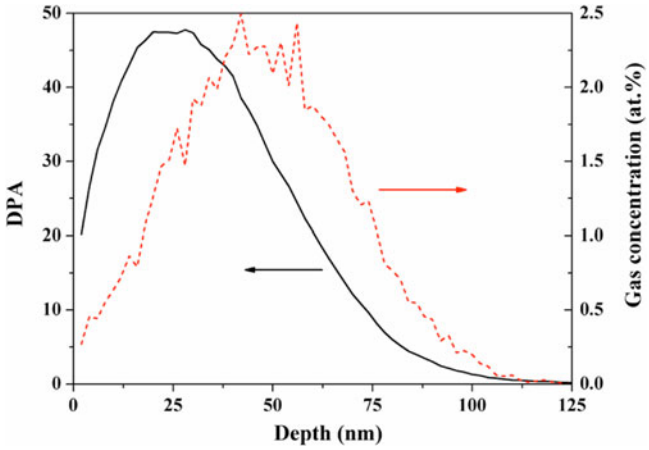

Fig. 1. The depth profile of radiation damage in units of dpa and krypton gas concentration obtained from SRIM simulation of CeO_2 subjected to 150-keV Kr ion irradiation at 600°C with a total dose of 1×10^{16} ions/cm^2.

III. RESULTS

The microstructure of CeO_2 after removing the Kr-implanted layer is shown in Fig. 2. Besides the dominant micrograins, some nanograin aggregates were also found in the sample, and they are mostly at triple and quadruple grain junctions of CeO_2 micrograins (Fig. 2a). The total amount of nanograins was estimated to be <1 vol % in the sample from a series of TEM images. The typical grain size of nanograins is in the range of 5 to 30 nm, and the average grain size for micrograins is ~5 μm. The diffraction pattern (inset in Fig. 2a) and EDS (Fig. 2b) confirm that these nanograins are also CeO_2. The additional Mo signal in EDS was from the Mo grid, which was used to hold a small piece of TEM foil cut from as-irradiated CeO_2 foil. Bright field images were taken at underfocus and overfocus conditions to confirm the presence of bubbles in the sample. Typically, small bubbles display as white and black spots at underfocus and overfocus conditions, respectively. However, there are no such features in the micrograins (Figs. 2c and 2d) and nanograins (Figs. 2e and 2f). The origin of these nanograins is currently not well understood, and possible causes are bimodal particle size distribution in the starting CeO_2 powders for preparing the pellets or inhomogeneous sintering of pellets. The grain growth mechanism during sintering is beyond the scope of this paper and will not be discussed here.

Figure 3a is a low-magnification TEM image of as-irradiated polycrystal CeO_2 up to an accumulated dose of 1×10^{16} ions/cm^2, which also shows the

[a]The polycrystalline CeO_2 pellets were purchased from Alfa Aesar, Ward Hill, Massachusetts.

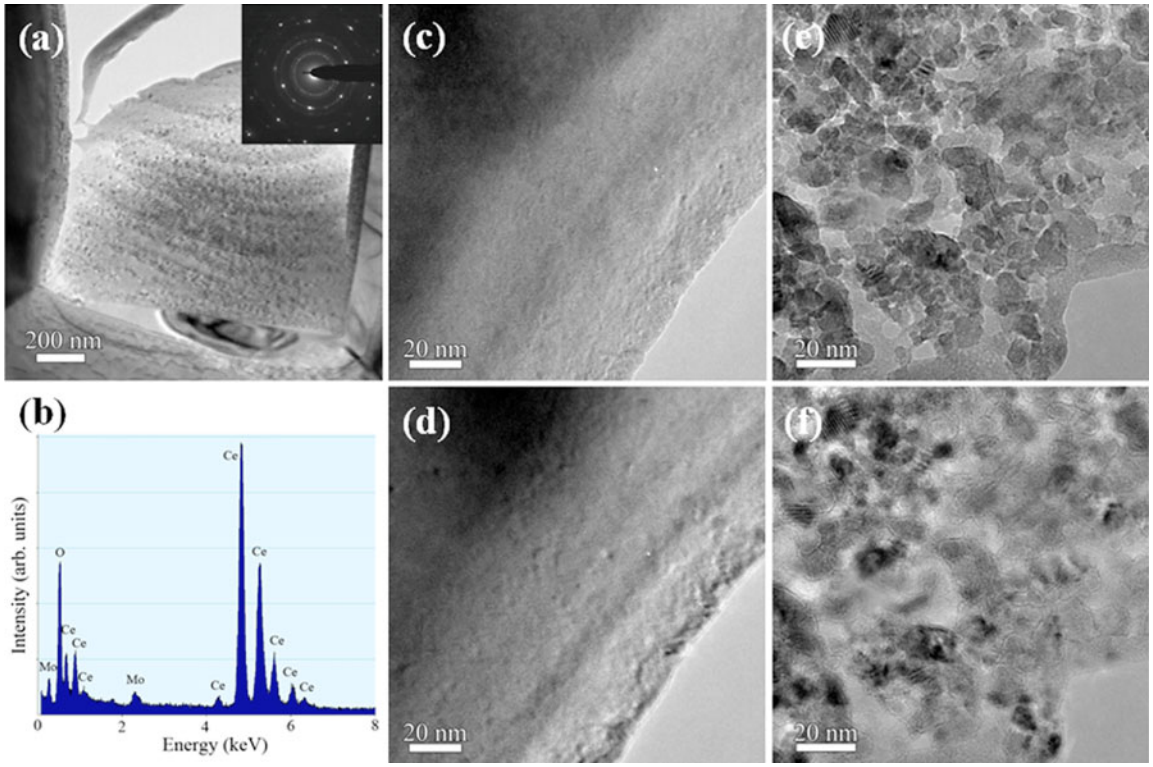

Fig. 2. Microstructure of polycrystalline CeO_2 after removing the Kr-implanted layer. (a) Typical CeO_2 nanograin region at the quadruple grain junction of micrograins (the inset shows the diffraction pattern). (b) EDS of CeO_2 nanograins. (c) Underfocus image for CeO_2 micrograin region. (d) Overfocus image for CeO_2 micrograin region. (e) Underfocus image for CeO_2 nanograin region. (f) Overfocus image for CeO_2 nanograin region.

coexistence of micrograins ("A" and "B") and nanograins ("C"). The magnified area of "C" is shown in Fig. 3b. The high-resolution TEM (HRTEM) image and diffraction pattern shown as insets in Fig. 3b indicate that there are many nanograins in the area marked "C" and their size is typically in the range of 10 to 30 nm. A dislocation network was observed in the micrograin region (Fig. 3a) and was found to be similar to that of single-crystal CeO_2 under the same irradiation condition,[10] but few dislocations were observed in the nanograin region (Fig. 3b). Uniformly distributed white spots and well-matched black spots at underfocus and overfocus conditions, respectively, were found for both micrograin regions (Figs. 3c through 3f) and nanograin regions (Figs. 3g through 3j), and they correspond to Kr bubbles. The bubbles at micrograin areas have an average diameter of 1.8 ± 0.3 nm and an area density of 4.7×10^{16} m^{-2}. The bubbles at the nanograin region have an average diameter of 1.4 ± 0.2 nm, which is relatively smaller than that at the micrograin region. Krypton and Xe bubbles with diameters of 1 to 2 nm were reported in single-crystal CeO_2 (Refs. 10 and 11) and polycrystalline UO_2 (Refs. 13 and 14) at similar temperatures and ion doses. In addition, the area density of the bubbles at the nanograin regions (3.4×10^{16} m^{-2}) is lower than that at the micrograin regions. Bubble swelling S_b was calculated according to Eq. (1):

$$S_b = \frac{\frac{1}{6}\pi \sum_i d_i^3}{st} \times 100\% \quad , \tag{1}$$

where

d_i = measured bubble diameter

s = total area for estimating the bubble number

t = average foil thickness.

By assuming t to be 20 nm for both the micrograin and the nanograin regions, we calculated the bubble swelling at the micrograin and the nanograin regions to be 0.79% and 0.28%, respectively, and the swelling ratio of the micrograin to the nanograin regions is close to 3. Table I summarizes the average bubble size and bubble linear density at the GB and in the bulk of the grain. In both the nanograin and the micrograin regions, the bubbles at the GB have statistically the same size as those in the bulk while the average linear density is higher at the GB.

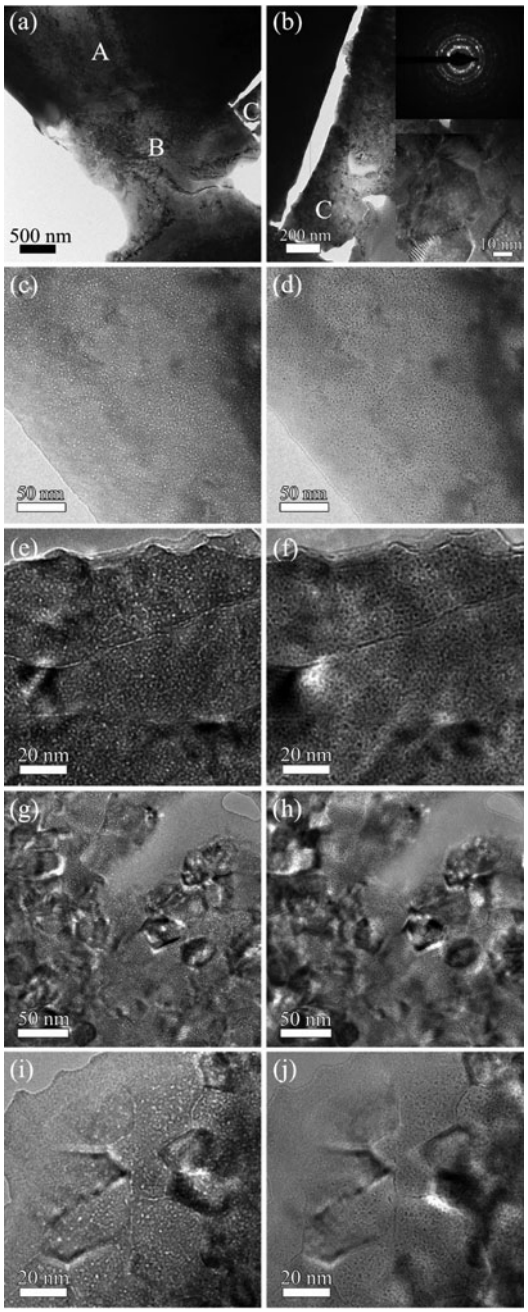

Fig. 3. Microstructure of polycrystalline CeO_2 irradiated with 150-keV Kr at 600°C up to a dose of 1×10^{16} ions/cm^2. (a) Micrograins ("A" and "B") coexist with nanograins ("C"). (b) Enlarged nanograin region of "C" (insets show the diffraction pattern and high-magnification TEM image for nanograins). (c) Underfocus image for CeO_2 micrograin region. (d) Overfocus image for CeO_2 micrograin region. (e) High-magnification underfocus image for CeO_2 nanograin region. (f) High-magnification overfocus image for CeO_2 micrograin region. (g) Underfocus image for CeO_2 nanograin region. (h) Overfocus image for CeO_2 nanograin region. (i) High-magnification underfocus image for CeO_2 nanograin region. (j) High-magnification overfocus image for CeO_2 nanograin region.

TABLE I

Summary of Bubble Size and Bubble Linear Density at GB and Bulk of Grain in Nanograin and Micrograin Regions

Region	Bubble Size (nm)	Bubble Linear Density ($\times 10^8$ m^{-1})
Bulk of nanograin	1.4 ± 0.2	1.6 ± 0.3
GB of nanograin	1.5 ± 0.3	2.7 ± 0.3
Bulk of micrograin	1.7 ± 0.2	2.1 ± 0.3
GB of micrograin	1.8 ± 0.2	3.1 ± 0.2

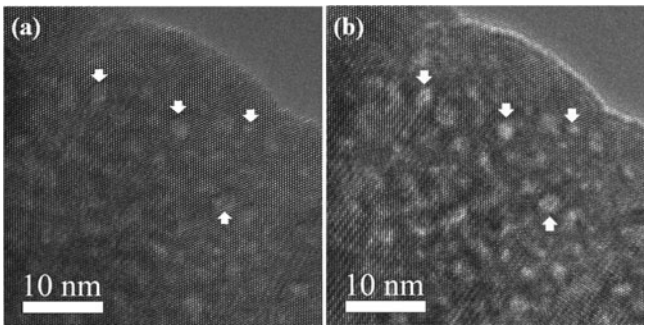

Fig. 4. CeO_2 grain irradiated with 150-keV Kr at 600°C up to a dose of 1×10^{16} ions/cm^2 when the electron beam is parallel to the [110] zone axis: (a) HRTEM image and (b) underfocus image. Some bubbles are marked by arrows.

Figure 4a shows the HRTEM image of Kr-implanted CeO_2, which was taken from the [110] zone. Figure 4b is the underfocus image of Fig. 4a. The round and light-colored features in Fig. 4a match well with the white ones in Fig. 4b, which corresponds to Kr bubbles. In addition, the lattice images show an insignificant difference in the bubble areas and the CeO_2 matrix, which indicates that there should be no solid Kr precipitates in the bubbles. Solid precipitates in bubbles were observed by Nogita and Une[15] in spent UO_2 fuel pellets with 45 to 83 GWd/ton. Nogita and Une found Moiré fringes within the bubble areas in the HRTEM images and extra spots in the diffraction patterns. In addition, solid Kr nanoclusters in MgO with Moiré fringes caused by the lattice mismatch between solid Kr and MgO were also revealed by the HRTEM image.[16] However, similar Moiré fringes were not found in the Kr bubbles in this work, which confirms the lack of solid precipitates.

IV. DISCUSSION

The reduction of radiation-induced swelling in nc oxide was first reported by Spino et al.,[2] who implanted,

125-keV Xe in YTZ at 800°C. The calculated bubble swelling ratio of large-grain 5YTZ to nc-4YTZ at a Xe dose of 5×10^{15} ions/cm^2 is ~3, which is identical to that of the micrograin region to the nanograin region in the present work. The reduction of radiation-induced swelling in nanostructured materials has also been predicted in recent literature.[17,18] Grain boundaries in a polycrystalline material have excess free volume (more open atom structure compared to perfect crystals).[19] As a result, the diffusivity of defects and Kr along GBs are considerably higher than those in bulk. Vacancies and interstitials have a higher probability of annihilation after being attracted to the GBs. Such annihilation processes could reduce the probability for the formation of vacancy clusters that could host Kr ions. Furthermore, higher mobility of Kr at GBs could reduce the localized Kr concentration in the bulk. Recently, theoretical modeling shows that besides the vacancy hopping processes to remove the vacancies from the bulk, interstitials at the GB can be emitted back to anneal the vacancies in the bulk.[18] The interstitial emission process has a much lower-energy barrier than conventional vacancy diffusion and can occur at a lower temperature.[18] This interstitial emission process would occur even at lower temperatures. These combined effects may explain the reduced swelling in the nanograin region. At micrograin regions, most vacancies and interstitials formed far away from the GB will have a lower probability of annihilation. Therefore, the vacancies have a greater probability to aggregate, trap implanted Kr ions, and form bubbles in the bulk of the grain. On the other hand, when the grain size approaches the migration distance of mobile point defects, the effect of the GB on microstructural development generally becomes significant. Recent molecular dynamics simulations[20,21] of radiation cascades in nc SiC showed that the total number of defects produced in a cascade increases with decreasing grain size mainly because of the increased volume fraction of the GB, and more defects are produced in the GB. However, the total number of defects produced in the crystalline parts of the material decreases with a decreasing grain size. Furthermore, once the number of defects is normalized with the volume of the crystalline regions, the total in-grain defect production is not significantly affected by the grain size.[21]

Dislocation loops and dislocations act as efficient sinks for interstitials and suppress the density of interstitials. Excess vacancies in the vicinity of dislocations aggregate easily and lead to bubble formation by trapping gas atoms. Therefore, the dislocation loops and dislocations at the micrograin region can induce higher gas bubble density. The mobility of interstitials is extremely high at a high temperature so that a large part of the interstitials may escape to the surface of the thin foils. In an extremely thin foil, or at positions very close to surfaces, the surface sink could become dominant and absorb the point defects.[22] In other words, the defects are difficult to accumulate at the edge areas of the foil, which results in the dislocation showing a much lower density and smaller size compared with defects at thick areas (Fig. 3). However, the surface sink strength for interstitials and vacancies at the micrograin and the nanograin regions should be comparable because of similar thicknesses.

Preferential accumulation of gas bubbles at the GB was observed in UO_2 fuel.[23] In simulations of polycrystalline materials, the gas atom formation energy is decreased within the GB and triple junction regions, which leads to preferential segregation and heterogeneous nucleation at these features.[24] On the other hand, the preferential nucleation and growth of Kr bubbles at the GB can result in a reduced Kr concentration at bulk. Figure 5 is a schematic diagram showing the bubble distribution comparison between the micrograin and the nanograin regions in CeO_2. Because of higher GB density in the nanograin region, the relative concentration of bubbles at GBs in the nanograin region should be higher compared to the micrograin region during irradiation (Figs. 5b and 5d). However, there was no evidence for a bubble-free zone next to the GB (Figs. 3e through 3j), which was occasionally observed in ion-implanted polycrystalline metals[25] and ceramics after postimplantation annealing at high temperatures.[26] Theoretical modeling shows that lower vacancy mobility and/or higher vacancy generation rates favor the formation of intragranular gas bubbles.[19] In the present work, the vacancy generation rate

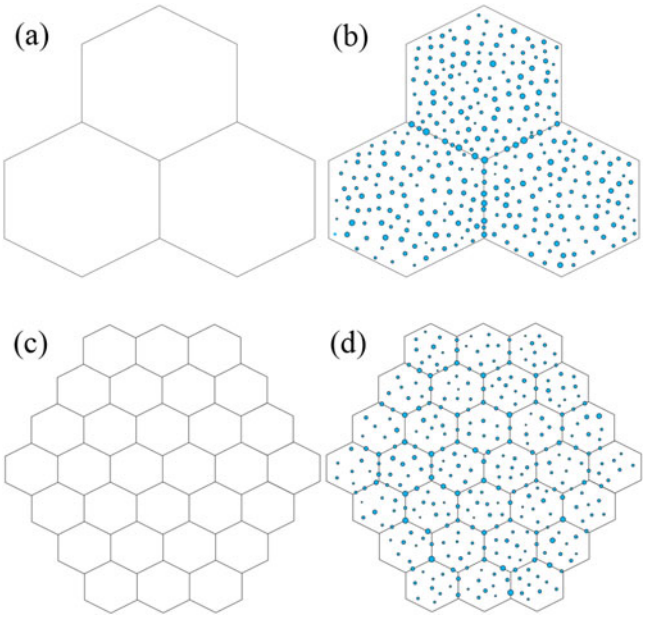

Fig. 5. Schematic diagram of the microstructure of bubbles at micrograin region [(a) and (b)] and nanograin region [(c) and (d)] in polycrystalline CeO_2 before implantation [(a) and (c)] and during implantation [(b) and (d)]. For simplicity, spherical bubbles instead of lenticular bubbles are used at GBs.

should be very high during Kr implantation, and the produced vacancies trapped Kr atoms quickly to form bubbles.

V. CONCLUSIONS

The microstructure of Kr bubbles in polycrystalline CeO_2 composed of both nanograins and micrograins was observed by TEM. The Kr bubbles exhibit smaller size and lower density at nanograin regions compared with micrograin regions. The lower-volume swelling of the nanograin region indicates that GBs are efficient sinks for defects induced by Kr ion bombardment. Grain boundaries are preferential sites for accumulation of Kr bubbles. There is no bubble-free zone next to the GBs mainly because of high vacancy generation rates under irradiation. No solid Kr precipitates in bubbles were revealed by the lattice images.

ACKNOWLEDGMENTS

This work was supported as part of the Center for Materials Science of Nuclear Fuel, an Energy Frontier Research Center funded by the U.S. Department of Energy (DOE), Office of Science, Office of Basic Energy Sciences. The Kr implantation was accomplished at the Electron Microscopy Center for Materials Research at ANL, a DOE Office of Science Laboratory operated under contract DE-AC02-06CH11357 by UChicago Argonne, LLC. This work has been completed in part using the facilities of the Microscopy and Characterization Suite at the Center for Advanced Energy Studies located in Idaho Falls, Idaho, and National Science Foundation–supported shared facilities at the University of Wisconsin.

REFERENCES

1. M. ROSE, A. G. BALOGH, and H. HAHN, "Instability of Irradiation Induced Defects in Nanostructured Materials," *Nucl. Instrum. Methods B*, **127–128**, 119 (1997).

2. J. SPINO et al., "Bulk-Nanocrystalline Oxide Nuclear Fuels—An Innovative Material Option for Increasing Fission Gas Retention, Plasticity and Radiation-Tolerance," *J. Nucl. Mater.*, **422**, 27 (2012).

3. A. MISRA et al., "The Radiation Damage Tolerance of Ultra-High Strength Nanolayered Composites," *JOM*, **59**, 62 (2007).

4. S. UKAI and M. FUJIWARA, "Perspective of ODS Alloys Application in Nuclear Environments," *J. Nucl. Mater.*, **307–311**, 749 (2002).

5. H. KLEYKAMP, "Selection of Materials as Diluents for Burning of Plutonium Fuels in Nuclear Reactors," *J. Nucl. Mater.*, **275**, 1 (1999).

6. Hj. MATZKE, V. V. RONDINELLA, and T. WISS, "Materials Research on Inert Matrices: A Screening Study," *J. Nucl. Mater.*, **274**, 47 (1999).

7. W. J. WEBER, "Alpha-Irradiation Damage in CeO_2, UO_2 and PuO_2," *Radiat. Eff.*, **83**, 145 (1984).

8. K. YASUNAGA et al., "Nucleation and Growth of Defect Clusters in CeO_2 Irradiated with Electrons," *Nucl. Instrum. Methods B*, **250**, 114 (2006).

9. K. YASUNAGA et al., "Electron Energy-Dependent Formation of Dislocation Loops in CeO_2," *Nucl. Instrum. Methods B*, **266**, 2877 (2008).

10. B. YE et al., "TEM Investigation of Irradiation Damage in Single Crystal CeO_2," *J. Nucl. Mater.*, **414**, 251 (2011).

11. B. YE et al., "The Effects of Xenon Implantation in Ceria with and Without Lanthanum," *Nucl. Instrum. Methods B*, **272**, 236 (2012).

12. J. F. ZIEGLER, U. LITTMARK, and J. P. BIERSACK, "Calculation Using the Stopping and Range of Ions in Matter (SRIM) Code"; http://www.srim.org/.

13. J. H. EVANS, "Effect of Temperature on Bubble Precipitation in Uranium Dioxide Implanted with Krypton and Xenon Ions," *J. Nucl. Mater.*, **188**, 222 (1992).

14. C. SABATHIER et al., "In Situ TEM Study of Temperature-Induced Fission Product Precipitation in UO_2," *Nucl. Instrum. Methods B*, **266**, 3027 (2008).

15. K. NOGITA and K. UNE, "High Resolution TEM of High Burnup UO_2 Fuel," *J. Nucl. Mater.*, **250**, 244 (1997).

16. M. A. VAN HUIS et al., "Formation of Solid Kr Nanoclusters in MgO," *Phys. Rev. B*, **67**, 235409 (2003).

17. G. ACKLAND, "Controlling Radiation Damage," *Science*, **327**, 1587 (2010).

18. X. M. BAI et al., "Efficient Annealing of Radiation Damage near Grain Boundaries via Interstitial Emission," *Science*, **327**, 1631 (2010).

19. S. HU et al., "Phase-Field Modeling of Gas Bubbles and Thermal Conductivity Evolution in Nuclear Fuels," *J. Nucl. Mater.*, **392**, 292 (2009).

20. F. GAO et al., "Energy Dissipation and Defect Generation in Nanocrystalline Silicon Carbide," *Phys. Rev. B*, **81**, 184101 (2010).

21. N. SWAMINATHAN et al., "Effects of Grain Size and Grain Boundaries on Defect Production," *Acta Mater.*, **58**, 2843 (2010).

22. C. KINOSHITA, K. HAYASHI, and S. KITAJIMA, "Kinetics of Point Defects in Electron Irradiated MgO," *Nucl. Instrum. Methods B*, **1**, 209 (1984).

23. I. ZACHARIE et al., "Microstructural Analysis and Modelling of Intergranular Swelling of an Irradiated UO_2 Fuel Treated at High Temperature," *J. Nucl. Mater.*, **255**, 92 (1998).

24. P. C. MILLETT, A. EL-AZAB, and D. WOLF, "Phase-Field Simulation of Irradiated Metals Part II: Gas Bubble Kinetics," *Comput. Mater. Sci.*, **50**, 960 (2011).

25. P. A. THORSEN et al., "Bubble Formation at Grain Boundaries in Helium Implanted Copper," *Scr. Mater.*, **51**, 557 (2004).

26. J. CHEN, Z. Y. HE, and P. JUNG, "Microstructure of Helium-Implanted α-Al_2O_3 After Annealing," *Acta Mater.*, **54**, 1607 (2006).